MORPHING AIRFOIL WITH ADAPTIVE BENDING-TWIST COUPLING

W. Raither[1], M. Heymanns[1], A. Bergamini[2], P. Ermanni[1]

[1]ETH Zürich, Centre of Structure Technologies, Leonhardstrasse 27, CH – 8092 Zürich

[2]Empa, Mechanics for Modelling and Simulation, Überlandstrasse 129, CH – 8600 Dübendorf

Abstract

A novel semi-passive morphing airfoil concept based on adaptive shear center location and torsional stiffness by means of smart materials is presented. Numerical parametric studies and upscaling show that the concept permits effective twist control while offering the potential of high lightweight and energy efficiency. By means of a scaled wing structure, effectivity and producibility of the structural concept are demonstrated experimentally.

1. INTRODUCTION

Aiming at smart roll control or at adaptive lift-to-drag ratio, some work has been done on the demonstration of the benefits of lifting surfaces with adjustable torsional stiffness [1] and on structural concepts that permit to put into effect the required changes in stiffness for wings [2, 3, 4, 5] or vertical tails [6]. However, the proposed solutions like moveable or rotary wing spars or a tail attachment with variable torsional rigidity are all based on rigid-body mechanisms and thus, as a matter of principle, they suffer from high weight, wear, particle release, proneness to errors and need for assembly as well as for lubrication [7].

Smart materials with variable stiffness like electro-bonded laminates [8, 9] or temperature-variable polymers [10, 11] represent alternatives to conventional mechanisms that promise to overcome not only these drawbacks, but also the conflict of requirements that is characteristic of shape-adaptable airfoils: While high stiffness is needed for carrying external loads, efficient shape adaptation requires a pronounced compliance.

Recent conceptual work on beams with rectangular cross section has shown the high potential of shape-adaptable lightweight structures based on the integration of smart materials with tunable stiffness: The bending-twist coupling behaviour of such beams with a variable-stiffness web can be adjusted in a wide range due to a powerful control of cross-sectional properties like torsional stiffness and shear center location [12]. The present work follows up on these previous findings, presenting a numerical and experimental evaluation of the mentioned concept when integrated in a wing structure.

2. CONCEPT

The morphing airfoil proposed here is based on the concept of adaptive bending-twist coupling presented in [12] for beams with rectangular cross section and is illlustrated in figure 1. One web of the profile – the right one shown in blue – is assumed to be constituted by a smart material of controllable shear stiffness. Let G_1 and G_2 denote the shear moduli of the constant part of the profile and of the adaptive-stiffness web, respectively, and let t_1 and t_2 denote the respective wall thicknesses. The symmetrical case is then given by the state in which the shear stiffness G_2t_2 of the adaptive web is equal to the shear stiffness G_1t_1 of the rest of the profile. In this case, the cross section's shear centre coincides with its centroid and, for the centered transverse loading shown in the figure, no torsion will occur. By activation of the smart material, the change in shear stiffness of the adaptive web will lead to a shift of the shear center in horizontal direction and thus to a non-zero twist of the profile. At the same time, the beam's torsional rigidity is changed. The bending stiffness, in contrast, is less affected by changes in the properties of one web, so that the influence on the beam's bending-twist coupling behaviour by activation of the adaptive web can be applied for controlling the twist and hence, in case of an aerodynamic surface, the lift forces.

The transfer of this working principle to an airfoil structure suggests the application of an adaptive wing box, so that the three-cell topology shown in figure 2 is assumed for the baseline configuration of the wing structure. Interfaces with variable shear stiffness are integrated at three different locations (numbers 1 to 3 in figure 2) for implementing adaptive coupling properties.

Changing the shear stiffness of interface 1 in the front spar of the wing box allows to shift the airfoil's shear center in horizontal direction and thus to change the torsional moment acting on the wing. At the same time, the torsional stiffness of the mid cell is varied. However, in order to substantially affect the wing's torsional rigidity, the behaviour of every cell has to be varied between the states represented by closed and open cross sections. Assuming the smart material to provide sufficient changes in shear stiffness, this condition is met by the integration of additional interfaces in the front cell (number 2) and in the rear cell (number 3), so that every cell of the airfoil can be reversibly "opened" and "closed".

During the operation of an airfoil transverse loads result from lift forces. For cambered airfoils, the point in which the resultant of these forces acts, i.e. the aerodynamic centre, is dependent on the angle of attack. At the current conceptual stage of this work, this is expected to be of secondary importance for the active principle of the concept, but it will have to be taken into account for the detailed design of any morphing airfoil based on this idea.

The variable shear stiffness G_2t_2 that is required for the activation of the adaptive web can in principle be achieved by changing either the web's shear modulus or its thickness. In the present work, an implementation based on the variation of the elastic modulus of a polymer web due to changes in temperature is investigated. In the range of their glass transition, the modulus of amorphous or semi-crystalline polymers typically drops with temperature by about three orders of magnitude within a temperature range of 20 to 30 K [13]. This thermomechanical behaviour is visualized in figure 29 for the polymer used in the frame of this work.

Concerning the transition from the two-dimensional section to a three-dimensional wing structure, an extension of the adaptive material over the whole span comes into question, as well as a partial integration. In this article only the complete extension is considered.

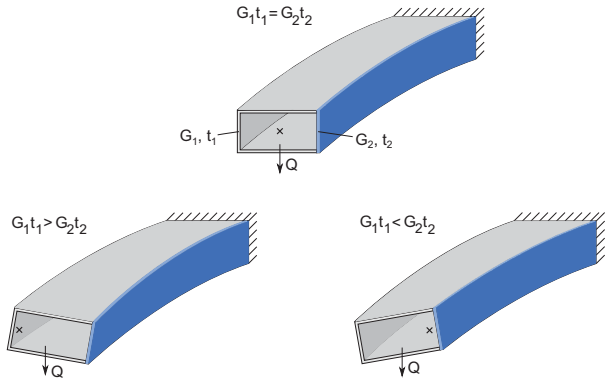

Figure 1: Working principle of adaptive beam

1, 2, 3: Interfaces with controllable shear stiffness

Figure 2: Schematic of a cross section of the adaptive airfoil

3. SIMULATION

In order to characterize the influence of geometric parameters on the mechanical behaviour of the adaptive airfoil, be able to implement a favourable design of the experimental wing structure discussed in section 4 and, finally, validate the measurements performed on this structure, a finite element model that simulates the elastic properties of the airfoil has been set up and evaluated. The following passages summarize the properties of the numerical model that several simulations have in common, while subsections 3.1, 3.2 and 3.3 contain characteristics which are specific for the respective analyses.

Figure 3 shows the geometrical parameters of a cross section of the NACA 0012 airfoil based on which the FE model is implemented and close-ups of the three variable-stiffness interfaces are presented in figure 4. The adaptive interfaces 1 and 3 are constituted by polymer layers in between overlaps of the spar plates and the upper and lower skin, respectively. Interface 2, in contrast, consists of a polymer bar which fills the gap in the lower skin and which is stepped in order to produce a smooth outer surface when attached to the protruding ends of the skin.

The numerical simulation is performed using the linear solver of “ANSYS” (release 12.0.1). The polymer parts, the stress state of which is expected to show a more pronounced three-dimensionality, are discretized into 20-node elements of the type “SOLID186”, while 4-node “SHELL181” elements (incompatible modes activated) are applied to model all of the other parts. The meshed finite element model is shown in figure 5, together with the system of coordinates that will be referred to in the following discussion.

Figure 6 presents the inner structure of the airfoil consisting, besides the spars, of ribs which equidistantly subdivide the airfoil along its span. The segmented open shape of these ribs (see figure 7 for a close-up) results from the requirement that they effectively reinforce the skin in bending and shear directions without considerably constraining the airfoil in warping direction, which is necessary to achieve a large drop in torsional stiffness for higher temperatures. All ribs are assumed to have the same thickness t_r, with the exception of the stronger load introduction rib at the tip that has a higher thickness t_{rt}.

As it is obvious from figure 6, the steps in the shape of interface 2 have been neglected in the finite element models, except for the one simulating the experimental wing structure.

In this work, the airfoil is assumed to be symmetric in spanwise direction, so that only one half of the wing can be considered that has a length L equal to half of the span and that is clamped at one side of the wing box. This boundary condition is implemented in the FE model by constraining all degrees of freedom of all nodes of the wing box for which $x = 0$.[1] With exception of an analysis covering the application of the concept in a wing of more realistic dimensions (see subsection 3.3), distributed aerodynamic lift loads are replaced by a substitute transverse force Q in z-direction[2] acting in the center of pressure. For simplicity reasons, the substitute load is introduced at the tip of the airfoil.

Assuming incompressible and inviscid flow over an airfoil section, the distance between the chordwise locations of neutral point and center of pressure is given by [14]

$$x_0 - x_p = \frac{c_m}{c_l} c \tag{1}$$

, c_m and c_l denoting the section’s moment coefficient with respect to the neutral point and its lift coefficient, respectively, and c denoting its chord length. With $x_0 = c/4$ and, as determined by means of the software “XFOIL” [15], $c_m = -0.007$ and $c_l = 0.603$, the location of the center of pressure reads $x_p = 0.262c$, so that the substitute lift Q has to be applied in $x = L$, $y = 0.262c$. Concerning the z-coordinate of this point of load application, the corresponding point on the upper part of the load introduction rib has been selected for every configuration.

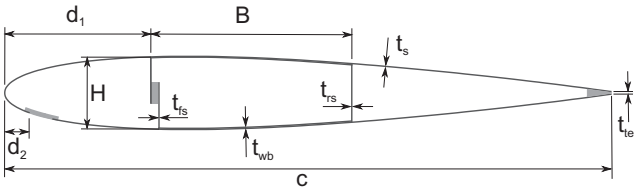

Figure 3: Geometry of a cross section

[1] As the experimental structure discussed later is clamped at the wing box only for practicality reasons, this boundary condition is also used for the numerical analyses, except for the ones related to upscaling.

[2] This is a good approximation only for small angles of attack, for which the substitute force defined in this way approximately points in the direction of the lift resultant.

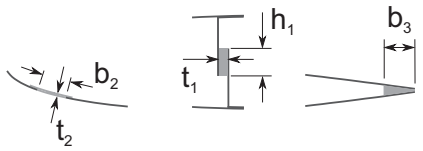

Figure 4: Geometry of the adaptive interfaces

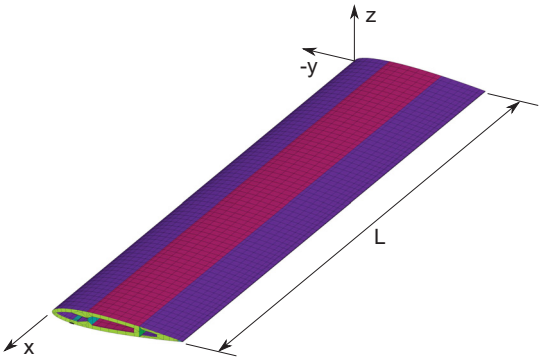

Figure 5: Finite element model and system of coordinates

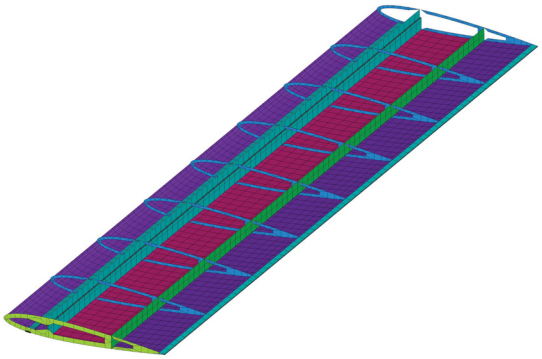

Figure 6: Implementation of ribs in the finite element model

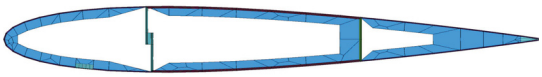

Figure 7: Close-up of a rib in the finite element model

3.1. Parametric Study

In order to assess the influence of the most important geometric parameters on the elastic behaviour of the adaptive airfoil, the finite element model is evaluated for different combinations of parameter values. Table 1 shows the values of the geometric parameters for the configuration used as a baseline for the parametric study, while the material properties used are reported in appendix A.1. Like in the case of the experimental wing structure, that is discussed later, the airfoil consists of carbon-fiber-reinforced polymer (CFRP), except for the spars that are executed in glass-fiber-reinforced polymer (GFRP), as the front spar has to serve as an electrical insulation for the resistive heating which is integrated in the experimental structure. The polymeric parts of the adaptive interfaces are assumed to consist of polyvinyl chloride (PVC).

As the experimental wing structure is supposed to be dimensioned for an ultimate transverse load of $Q_{\max} = 90\,\mathrm{N}$ in the soft state – for which a value of $E_{\min} = 12\,\mathrm{MPa}$ is assumed as minimum Young's modulus of the polymer layers –, also the baseline configuration for the parametric study is designed according to this requirement. Stability being the most critical design criterion, wall thicknesses and rib distance are chosen in a way that the smallest buckling load for a polymer modulus of $E_{\min}$ in all interfaces – which represents the most compliant and thus the most critical state – equals $Q_{\max}$.

The parametric study considers following parameters as variables:

- The number of activated adaptive interfaces,
- B/c, the width of the wing box, normalized by the chord length,
- d_1/c, the offset of the wing box, normalized by the chord length,
- h_1/H, the height fraction of interface 1,
- t_1/t_s, the thickness of interface 1, normalized by the thickness of the skin,
- b_2/c, the width of interface 2, normalized by the chord length,
- d_2/c, the offset of interface 2, normalized by the chord length,
- t_2/t_s, the thickness of interface 2, normalized by the thickness of the skin,
- b_3/c, the width of interface 3, normalized by the chord length.

During the variation of the dimensionless parameters, c and t_s are held constant.

The number of ribs (including the tip rib) is nine for the parametric study.

Parameter	Unit	Value
L	mm	1300
c	mm	300
B	mm	120
t_{wb}	mm	1.2
t_{fs}	mm	1.25
t_{rs}	mm	1.25
t_s	mm	0.6
t_r	mm	1.05
t_{rt}	mm	1.75
t_{te}	mm	0.75
d_1	mm	80
h_1/H	-	0.2
t_1/t_s	-	5
d_2	mm	40
b_2	mm	10
t_2	mm	2
b_3	mm	10

Table 1: Geometrical parameters of the baseline geometry for the parametric study

3.2. Simulation of Experimental Wing Structure

The target values of the basic geometrical parameters in the experiment are the same as the ones of the baseline configuration used for the parametric study. However, compared to the more ideal geometry presumed for the parametric study, the following characteristics of the real experimental wing structure are included for the simulation of the latter:

- The actual values of the wall thicknesses measured at the experimental structure,
- The stepped shape of interface 2,
- CFRP heating stripes in all interfaces,
- Stripes made of aramide-fiber-reinforced plastic (AFRP) for the purpose of thermal insulation in all interfaces,
- Overlaps of the spars and the flanges of the wing box,
- Bonding layers between these flanges and spars, between the flanges and the skin and in interface 2,
- A protrusion of the skin at the tip of the wing structure by 5 mm with respect to the mid of the load introduction rib (the length L is defined as the distance between clamping and mid of the load introduction rib).
- The additional heating and insulation stripe on the left side of interface 1 which is shown in figure 9 and which is present to replace the one more on the right side which suffered damaged during the first tests,
- A 0.15 mm thick layer of paint (consisting of a 0.1 mm epoxy primer and a 0.05 mm polyurethane varnish) covering the outer surface of the wing.

These particularities are illustrated in figures 8 and – as a close-up of the adaptive interfaces – 9 and the respective total thicknesses and overlap widths are specified in table 2. The values of thickness of heating and insulation stripes are given in table 3.

For CFRP, GFRP and PVC, the material properties of appendix A.1 are used. Additional material properties related to the mentioned extensions are given in appendix A.2. For both CFRP and AFRP stripes, [0°; 90°] fabric is used as reinforcement.

Additional differences between parametric study and experiment are given by the higher number of ribs of eleven in the experimental structure and by the tip rib that has a different lay-up[3] and a higher thickness of $t_{rt} = 2.34\,\mathrm{mm}$ in case of the experiment.

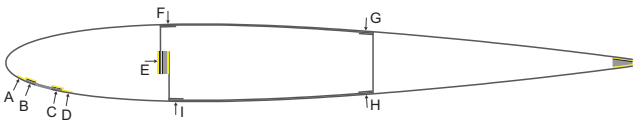

Figure 8: Geometry of a cross section of the experimental wing structure

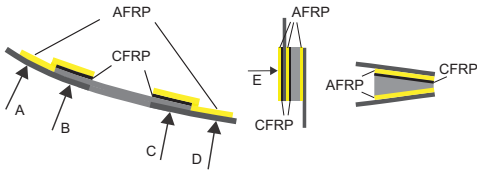

Figure 9: Geometry of the adaptive interfaces of the experimental wing

Location	Overall Thickness [mm]	Overlap width [mm]
A	2.71	14.1
B	3.79	9.26
C	3.73	9.6
D	2.66	14.5
E	7.86	7
F	3.1	15.5
G	2.95	15.2
H	2.95	16.3
I	4.33	15.2

Table 2: Geometrical parameters of the experimental wing structure

Part	Thickness [mm]
AFRP insulation stripe	0.51
CFRP heating stripe	0.33
AFRP/CFRP combined stripe[4]	0.74

Table 3: Thickness of heating and insulation stripes

3.3. Upscaling to Realistic Conditions

With the intention of investigating the performance of the proposed concept in a wing which can be considered as more realistic in terms of dimensions and loading, an upscaled finite element model is evaluated.

For the upscaling, a non-swept rectangular wing with a NACA 2412 section, a chord of $c = 0.6\,\mathrm{m}$, a span of $2L = 15\,\mathrm{m}$ and hence an area of $A = 2cL = 9\,\mathrm{m}^2$ is chosen. For each part, the stacking sequence of its laminate is the same as the respective one of the parametric study reported in appendix A.1, but all ply thicknesses are scaled up by a factor of eight, so that all wall thicknesses are also scaled up by eight[5]. The values of the remaining geometrical parameters of the upscaled wing are given in table 4. A total of 24 ribs is applied in the upscaled wing.

Concerning the flight conditions, the calculations are performed assuming a steady-state horizontal flight in an incompressible and inviscid flow, a flow velocity of $v = 41\,{}^{m}/_{s}$ and a total airplane mass of $m = 415\,\mathrm{kg}$. In terms of wing span and area, flight speed and mass, these considerations are representative of a glider of the FAI 15 meter competition class like, for example, the Schleicher ASW 27 [16].

[3] [90°; 45°; -45°; 45°; -45°; 0°; -45°; 45°; -45°; 45°; 90°] wrt to global y-axis.
[4] For all cases where a heating layer is in contact with an insulating layer.
[5] This scaling factor of eight leads to the reasonable value of three for the smallest buckling factor of the upscaled wing, given an interface modulus of 100 MPa.

Equilibrium under these conditions requires a lift coefficient of

$$c_L = \frac{mg}{\frac{\rho}{2} v^2 A} = 0.44 \tag{2}$$

where $g = 9.81\,{}^{m}/_{s^2}$ denotes gravitational acceleration and, concerning the air density, the value of $\rho = 1.225\,{}^{kg}/_{m^3}$ (standard atmosphere at sea level [14]) is assumed.

Figure 10 shows the way in which the aeroelastic calculations are performed. The iteration cycle involves ANSYS for the determination of the twist distribution in the elastic domain and, in a sub-loop for every spanwise coordinate where nodes are placed in the FE model, XFOIL for calculating the two-dimensional pressure distribution for each airfoil section and a lifting line method [17] to take into account the three-dimensional pressure distribution due to the finite span of the wing. Finally, MATLAB is used to run the iteration. For these calculations, an angle of attack of two degrees is presumed.

In order to compare the potential performance of the adaptive concept when applied for roll control with the one of a conventional control surface, the roll moment coefficient

$$c_{L_{\text{roll}}} = \frac{L_{\text{roll}}}{AL\frac{\rho}{2}v^2} \tag{3}$$

is evaluated, where

$$L_{\text{roll}} = -\int_{-L}^{L} c_l \frac{\rho}{2} v^2 c x \, dx \tag{4}$$

represents the rolling moment. In the last equation, c_l denotes the lift coefficient of a section of the airfoil.

Conventional ailerons covering the whole span and 17% of the chord serve as a reference configuration for this comparison. Corresponding to the antimetric deflection of these ailerons, also the smart system is assumed to generate antimetric changes in lift.

For every analysis related to the upscaling, all the three interfaces are supposed to be active and to exhibit the same temperature. Furthermore, for the determination of divergence speed, shifting of the aerodynamic center is considered as a secondary effect and is hence neglected.

Parameter	Unit	Value
L	mm	7500
c	mm	600
B	mm	240
t_{te}	mm	1.5
d_1	mm	160
${}^{h_1}/_{H}$	-	0.2
${}^{t_1}/_{t_s}$	-	5
d_2	mm	80
b_2	mm	20
t_2	mm	4
b_3	mm	20

Table 4: Geometrical parameters of upscaled wing

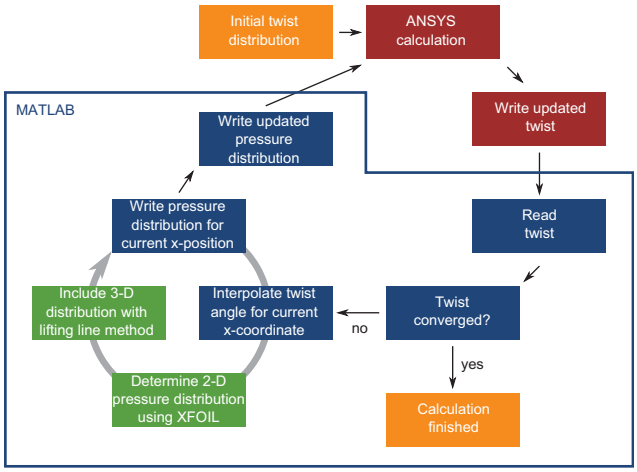

Figure 10: Iteration procedure for aeroelastic calculations

4. EXPERIMENT

Figure 11: Experimental wing structure

Figure 12: Inner structure of experimental wing

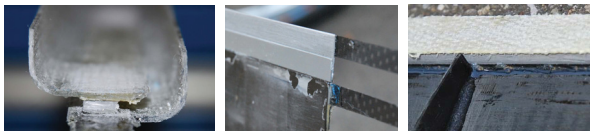

(a) Interface 1 (b) Interface 2 (c) Interface 3

Figure 13: Close-ups of the adaptive interfaces before closure of the experimental wing structure

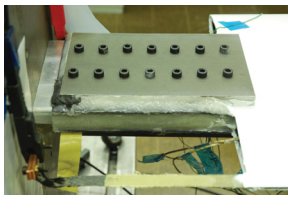

Figure 14: Clamping of the experimental wing structure

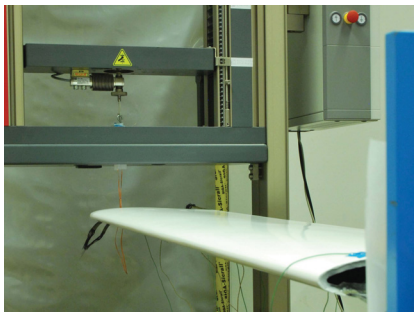

Figure 15: Application of loads to the experimental wing structure

In order to validate the numerical results and to demonstrate the feasibility of the integration of the proposed structural concept in a real structure, an experimental wing structure has been manufactured and tested.

The experimental airfoil structure exhibits the geometrical characteristics discussed in subsection 3.2. Also its material properties and laminate stacking sequences are the ones already mentioned (see subsection 3.2 and appendices A.1 and A.2).

The skin of the airfoil structure, its wing box flanges and its ribs are made of the “Toho Tenax HTS40”/“ACG MTM 44-1” unidirectional carbon fiber/epoxy prepreg, while glass fiber fabric and epoxy are applied for the spars. The rear spar is made using a VARI process and the front one is produced by wet lay-up. Auxiliary parts are made by VARI processing (fastening angles) and wet lay-up (heating and insulation stripes), as well. While “Huntsman Araldite LY 5052/Aradur 5052” is applied for these supplementary items, all the other parts are made using “Epoxy resin L” and “Hardener EPH 161” by “R&G Faserverbundwerkstoffe”. All bondings are also based on “Huntsman Araldite LY 5052/Aradur 5052” and hard PVC is employed for the realization of the adaptive interfaces. Subsequently to the assembly of all the parts, the outer surface of the wing structure is filled, sanded and painted with epoxy primer and polyurethane varnish.

For the purpose of clamping, the wing box protrudes in negative x-direction by 17 cm at its root, where it is fixed to a support by means of an aluminium core and steel plates which are bolted from the exterior, as apparent from figure 14. At the tip, a transverse load of $Q = 11\,\mathrm{N}$ is exerted to the load introduction rib by a “Zwick Z005” tensile testing machine equipped with a 100 N load cell. In order to determine flexural and torsional deformations, deflections w in z-direction are measured on the lower outer surface, at the spanwise location of the load introduction rib ($x = L$) and at the two chordwise positions of the spars ($w_{1,\,\mathrm{tip}}$ at the front spar, $w_{2,\,\mathrm{tip}}$ at the rear spar) using two triangulation laser sensors. At every position and for each temperature, seven measurements are performed.

A current source is connected to the heating stripes of each adaptive interface for individual heating and, for the purpose of temperature monitoring and feedback control of the current sources, a total of 22 thermocouple sensors are placed on the interfaces (see appendix A.2 for the exact locations). Data acquisition and temperature control are implemented using a “LabVIEW” program.

Photographs of the experimental wing structure are shown in figures 11 to 15.

5. RESULTS

5.1. Parametric Study

The following subsections show the results of the parametric study, considering deflections $w_{\mathrm{S},\,\mathrm{tip}}$ of the shear center and twist angles φ_{tip}, both at the tip of the airfoil structure. For subsections 5.1.2 to 5.1.5, all three variable-stiffness interfaces are considered to be active and to exhibit the same elastic modulus.

5.1.1. Combination of Adaptive Interfaces

In figure 16, relative shear center position $\frac{y_S}{c}$, as well as normalized deflection and twist are plotted with respect to the elastic modulus E_{adapt} of the adaptive interfaces for different combinations of activated interfaces.

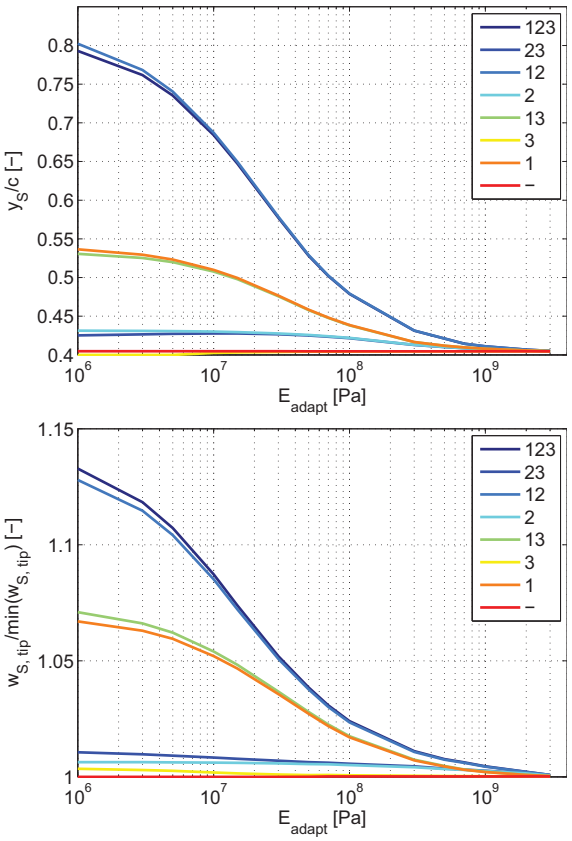

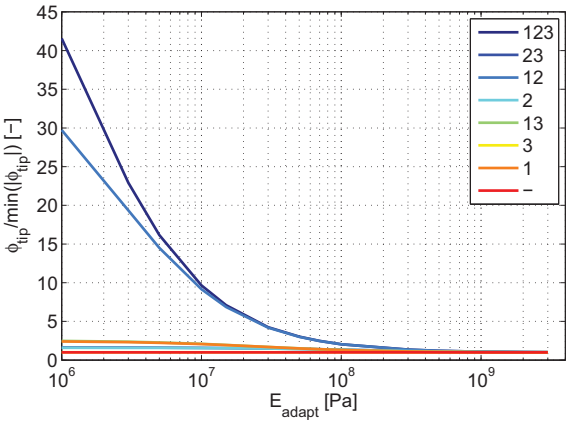

Figure 16: Influence of the combination of activated adaptive interfaces (indicated by the numbers in the legends) on normalized shear center position, deflection and twist

5.1.2. Offset and Width of Wing Box

Figure 17 visualizes the effect of normalized width and offset of the wing box on the coupling ratio for different values of elastic modulus of the variable interfaces.

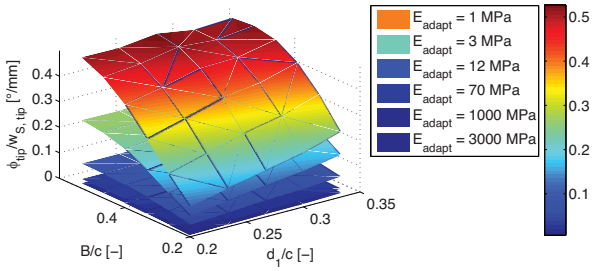

Figure 17: Influence of normalized offset and width of the wing box on coupling ratio

5.1.3. Height Fraction and Thickness of Interface 1

The influence of the main characteristics of interface 1, namely its height fraction and its relative thickness, on the coupling behaviour is shown by figure 18.

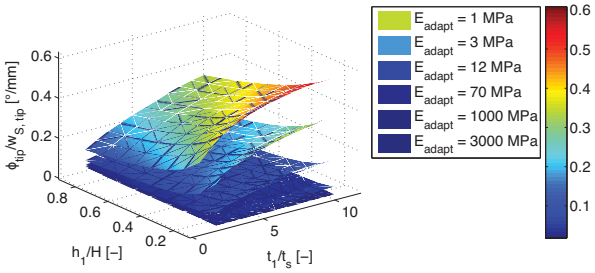

Figure 18: Influence of height fraction and relative thickness of interface 1 on coupling ratio

5.1.4. Offset and Width of Interface 2

Figure 19 shows the result of a parametric study considering the sensitivity of the coupling ratio on variations of non-dimensional offset and width of interface 2.

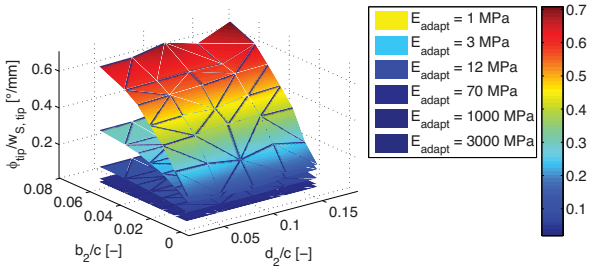

Figure 19: Influence of normalized offset and width of interface 2 on coupling ratio

5.1.5. Thickness of Interface 2 and Width of Interface 3

In figure 20, the influence of the thickness of the front interface and of the width of the rear one is shown.

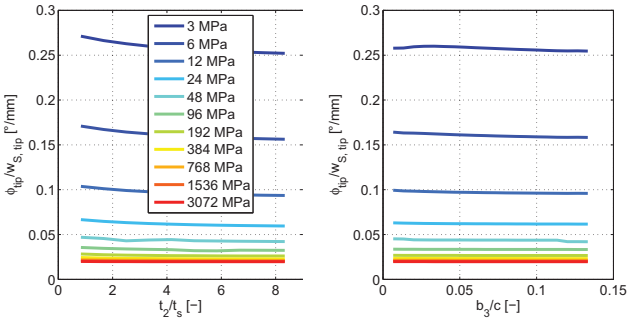

Figure 20: Influences of relative thickness of interface 2 and of relative width of interface 3 on coupling ratio for different values of E_{adapt}

5.2. Comparison of Numerical and Experimental Results

Deflection compliance and torsional compliance as determined by experiment and simulation are plotted against interface temperature in figures 21 and 22, respectively, while figure 23 shows the coupling ratio calculated from these results and based on the deflection $w_{0,\mathrm{tip}}$ at the chordwise location of the centroid of the wing box[6]. The experimental results are plotted as mean values resulting from different measurements and vertical error bars accordingly represent standard deviations. Inhomogeneous temperature distributions are taken into account by the respective standard deviation of the measured values of all thermosensors which is specified for every data point by a horizontal error bar.

[6] Precisely, the mean value of the displacement values of both sensors has been used, which approximately equals the displacement at the chordwise center.

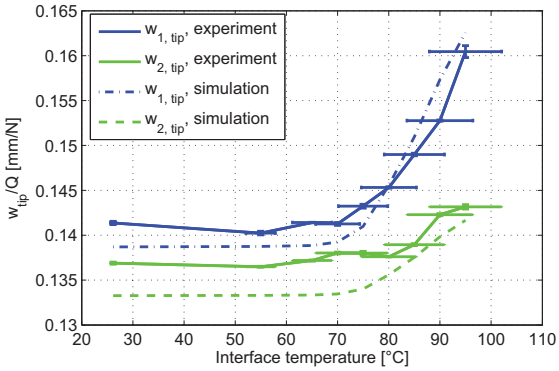

Figure 21: Deflection compliance at the tip against interface temperature – comparison between experiment and simulation

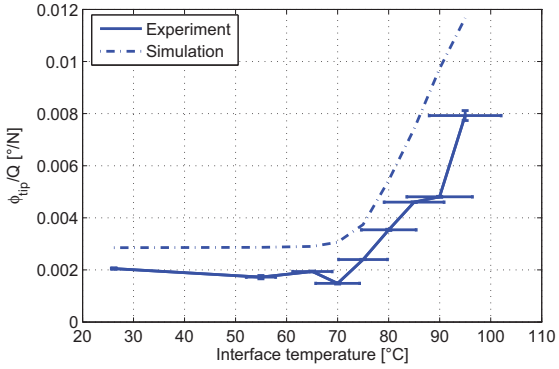

Figure 22: Torsional compliance at the tip against interface temperature – comparison between experiment and simulation

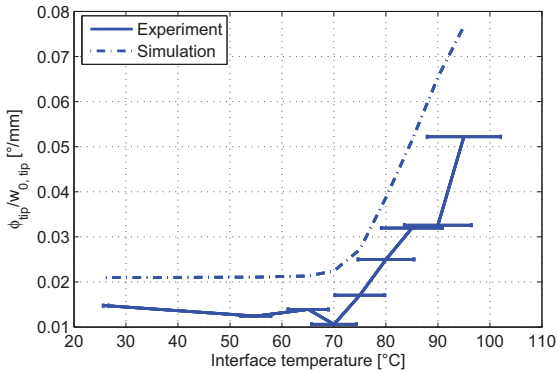

Figure 23: Coupling ratio at the tip against interface temperature – comparison between experiment and simulation

5.3. Upscaling to Realistic Conditions

In figure 24, the twist moment equilibria resulting from the aeroelastic analysis for different interface states are shown and figure 25 contains a plot of the wing's lift coefficient against the interface modulus. The wing's twist angle distribution is shown in figure 26 for different elastic moduli of the adaptive interfaces, while in figure 27 the influence of interface stiffness on divergence speed is presented. By means of figure 28, finally, the variation in roll moment coefficient resulting from an adaptation of the variable-stiffness interfaces is compared to the one achieved by conventional aileron deflection.

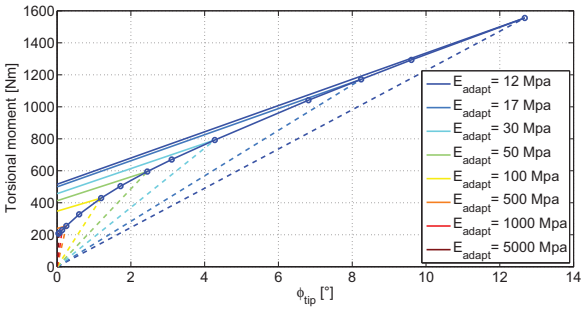

Figure 24: Aeroelastic equilibria for different interface states

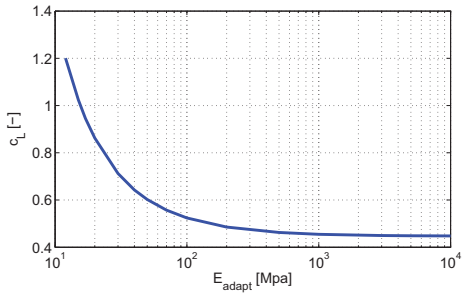

Figure 25: Lift coefficient with respect to interface modulus

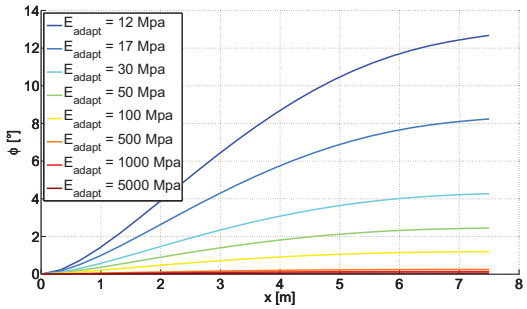

Figure 26: Wing twist distribution for different interface states

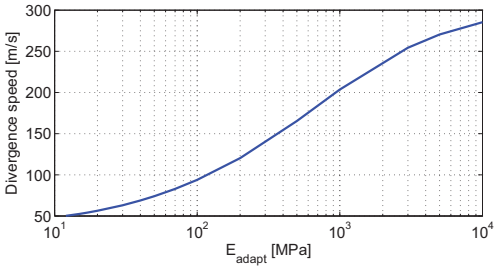

Figure 27: Divergence speed with respect to interface modulus

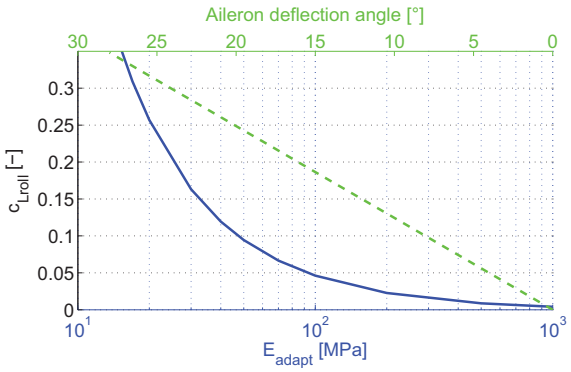

Figure 28: Comparison of roll moment coefficients due to interface activation (blue solid line) and aileron deflection (green dashed line)

6. DISCUSSION

The airfoil structure's expected behaviour of adaptive bending-twist coupling is well apparent from both numerical and experimental results. For all configurations, large changes in coupling ratio can be achieved, as the torsional stiffness is much more dependent on the state of the adaptive interfaces than the flexural one.

As shown by the parametric study, the change in coupling stiffness is especially pronounced for the case of a relatively wide wing box and a shear center position that is relatively far behind the one of the aerodynamic center. Furthermore, for all adaptive interfaces, a larger amount of variable-stiffness material generally leads to a broader adaptation range, as the effect of these interfaces on the twist of the airfoil is much bigger than the one on its bending. However, interface 1 provides the largest stiffness changes if it is designed to have a small height and a large thickness, so that the shear stiffness in the more compliant states is low. Additionally, it has to be mentioned that also a smaller thickness of interface 2 and a smaller width of interface 3 lead to higher ranges of coupling ratio due to a favourable influence on the compliance in the softer states, although the effect of both parameters is comparably small. Concerning the respective influence of the single interfaces, interface 1 is most effective due to its big impact on the shear center position, but in order to put into effect considerable changes in coupling stiffness at least interface 2 has to be activated additionally to "open" and "close" the front cell which significantly contributes to the torsional stiffness.

Experimental and numerical results agree well in qualitative and, as far as the deflection is concerned, also in quantitative terms, the relative error of the simulation with respect to the experiment staying within five percent. However, when it comes to a quantitative comparison of the twist angles, higher deviations are present, which is not surprising for this derived quantity. Due to the strong coupling of thermal and mechanical properties that is in the nature of the concept discussed here, there are manifold potential reasons for these deviations: First of all, the homogeneous temperature distribution assumed for the simulation is not present in the experiment, as obvious from the large variance of the temperature values. Furthermore, uncertainties related to the widely scattering material properties of the applied composite materials and to geometrical properties, followed by smaller discrepancies in temperature and displacement measurement are considered to be probable sources of errors. Also the thermomechanical behaviour of the applied resins and adhesives, that is not accounted for in the simulation, can – in spite of the high glass transition temperatures of these materials [18, 19, 20] – lead to an additional softening in the experiment, which could explain a certain part of the deviations.

The numerical upscaling points out that, as a matter of nature, reductions in interface stiffness lower the divergence velocity. Nevertheless, it is shown by the analyzed example airfoil that designs based on the proposed concept are possible which provide sufficient changes in lift coefficient while being stable in terms of static aeroelasticity. In fact, in case of the presented design, divergence is not critical for any interface state due to prior occurrence of stall. The values of roll moment coefficient that are possible by activation of the smart system are of the same order as the ones achieved by conventional aileron deflection in case of the analyzed airfoil.

7. CONCLUSIONS AND OUTLOOK

It has been verified by simulation and experiment that the concept of variable shear center location and variable torsional stiffness can be integrated into an airfoil structure to realize an adaptively bending-twist coupled morphing wing. Furthermore, it has been shown by a numerical upscaling that the concept in principle permits changes in lift that are of sufficient quantity to be applied, as an example, for roll control in a wing of an airplane. Being compliant and providing continuous shape changes, it is expected to allow for advances in lightweight efficiency as well as in aerodynamic performance when compared to conventional control surfaces.

Due to its semi-passive nature – apart from the relatively small amount of energy that has to be spent for the activation of the adaptive interfaces, the energy required for the shape adaptation is extracted from the aerodynamic loads – the concept promises high energy efficiency and great lightweight potential. However, instead of the thermal solution investigated here, electro-bonded laminates should be applied that offer variable stiffness at still lower energy expense. An electrostatic solution is favourable not only in this respect, but also in terms of activation speed and independence from varying operational temperatures that are both decisive for the applicability of the structural concept.

Changes in roll moment coefficient of the same order as the ones due to conventional aileron deflection are possible by activation of the smart system for the case of the analyzed airfoil. However, the moment characteristic is generally nonlinear with respect to steering inputs, which might pose higher demands on flight control.

A synergetic combination of the effects of adjustable shear center location and variable torsional stiffness requires the stiffness to decrease during every shape adaptation. In order to implement reversible twist angles, reverse shifting of the shear center has thus to be put into effect, for example by provision of an additional adaptive interface in the rear spar of a morphing wing design based on the presented concept.

Further aspects like the integration of electro-bonded laminates or a more realistic aeroelastic analysis covering flutter and stall as well as viscous and compressible effects go beyond the scope of this work, but should be addressed by future research for a deeper investigation of the concept's potential of application in shape-adaptable wings.

A. MATERIAL PROPERTIES

A.1. Parametric Study

Structural element	Material	Stacking angles [°]	Thickness [mm]
Wing box flanges	CFRP (UD)	[[0; 90]s]s	1.2
Front spar	GFRP (fabric)	[0; 0; 45; 0; 0]	1.25
Rear spar	GFRP (fabric)	[0; 0; 45; 0; 0]	1.25
Skin	CFRP (UD)	[0; 90]s	0.6
Ribs	CFRP (UD)	[90; 45; -45; 0; -45; 45; 90] (wrt to global y-axis)	1.05
Tip rib	CFRP (UD)	[90; 45; -45; 0; -45; 45; 90] (wrt to global y-axis)	1.75

Table 5: Laminate lay-up for parametric study

Property	Unit	Value[7]
E_{11}	GPa	94.4
E_{22}	GPa	6.45
G_{12}	GPa	3.77
ν_{12}	-	0.27
G_{23}	GPa	2.69

Table 6: Transversely-isotropic properties of unidirectional CFRP layer

Property	Unit	Value[8]
E_{11}=E_{22}	GPa	23.8
G_{12}	GPa	3.41
ν_{12}	-	0.11
G_{23}	GPa	2.60

Table 7: Orthotropic properties of bidirectional GFRP layer (fabric as reinforcement)

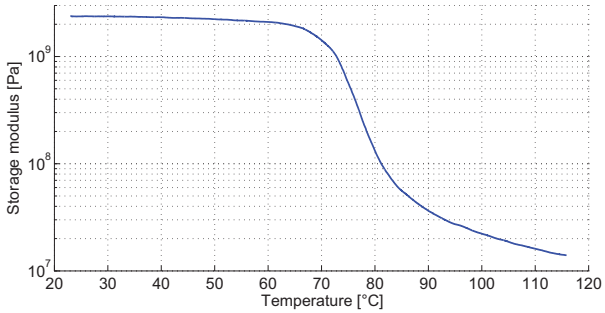

Figure 29: Temperature-dependent elastic modulus of PVC

The elastic modulus E of PVC shown in figure 29 has been measured by DMA and corrected by the value determined for room temperature by static tensile tests close to the conditions specified by DIN EN ISO 527 [24, 25].

Concerning the temperature dependence of the Poisson ratio of PVC, the following model has been applied [26]:

$$\nu = \nu|_{T=23℃} + \left(0.5 - \nu|_{T=23℃}\right)\left(1 - \frac{E}{E|_{T=23℃}}\right) \quad (5)$$

where $\nu|_{T=23℃} = 0.38$ [27].

A.2. Experiment

Property	Unit	Value[9]
E_{11}=E_{22}	GPa	34.7
G_{12}	GPa	1.88
ν_{12}	-	0.05
G_{23}	GPa	1.92

Table 8: Orthotropic properties of bidirectional AFRP layer (fabric as reinforcement)

Property	Unit	Value[10]
E_{11}=E_{22}	GPa	95.4
G_{12}	GPa	3.87
ν_{12}	-	0.023
G_{23}	GPa	3.09

Table 9: Orthotropic properties of bidirectional CFRP layer (fabric as reinforcement)

Property	Unit	Value (bonding and primer)[11]	Value (varnish)[12]
E	GPa	3.5	1.6
ν	-	0.35	0.30

Table 10: Isotropic properties of bonding, primer and varnish

[7] The first four values are test results taken from [11], the transverse shear modulus is based on a correction of the in-plane shear modulus according to the data base of [21].

[8] These values are determined by application of the rule of mixture proposed in [22], the fiber values being taken from [23] and the matrix values being the ones specified by the manufacturer [19].

[9] Taken from the data base of [21].

[10] Taken from the data base of [21].

[11] [19].

[12] [28].

Interface number	Spanwise positions of temperature sensors [cm]
1	2.2; 20.2; 38.2; 56.2; 74.2; 92.2; 110.2; 128.2
2	0.75; 22.25; 43.75; 65.25; 86.75; 108.25; 129.75
3	0.5; 34; 49; 64; 81; 98; 130

Table 11: Positions of temperature sensors

References

[1] K. E. Griffin and M. A. Hopkins, "Smart stiffness for improved roll control," in *AIAA 36th Structures, Structural Dynamics and Materials Conference*, 1995.

[2] P. C. Chen, D. Sarhaddi, R. Jha, D. D. Liu, K. Griffin, and R. Yurkovich, "Variable Stiffness Spar Approach for Aircraft Maneuver Enhancement Using ASTROS," *Journal of Aircraft*, vol. 37, no. 5, pp. 865–871, 2000.

[3] M. Amprikidis and J. E. Cooper, "Experimental validation of wing twist control using adaptive internal structures," in *45th AIAA/ASME/ASCE/AHS/ASC Structures, Structural Dynamics & Materials Conference*, 2004.

[4] J. E. Cooper, "Adaptive Stiffness Structures for Air Vehicle Drag Reduction," in *Multifunctional Structures/Integration of Sensors and Antennas. Meeting Proceedings RTO-MP-AVT-141*, 2006.

[5] R. M. Ajaj, M. I. Friswell, W. G. Dettmer, G. Allegri, and A. T. Isikveren, "Conceptual modeling of an adaptive torsion wing structure," in *52nd AIAA/ASME/ASCE/AHS/ASC Structures, Structural Dynamics and Materials Conference*, 2011.

[6] M. Amprikidis, J. E. Cooper, and O. Sensburg, "Development of an adaptive stiffness all-moving vertical tail," in *45th AIAA/ASME/ASCE/AHS/ASC Structures, Structural Dynamics & Materials Conference*, 2004.

[7] L. F. Campanile, "Lightweight Shape-Adaptable Airfoils: A New Challenge for an Old Dream," in *Adaptive Structures: Engineering Applications*, D. Wagg, I. Bond, P. Weaver, and M. Friswell, Eds. Chichester: John Wiley & Sons, 2007, pp. 89–135.

[8] A. Bergamini, R. Christen, B. Maag, and M. Motavalli, "A sandwich beam with electrostatically tunable bending stiffness," *Smart Materials and Structures*, vol. 15, pp. 678–686, 2006.

[9] L. Di Lillo, W. Raither, C. Di Fratta, A. Bergamini, and P. Ermanni, "Mechanical characterization of electrobonded laminates," in *ASME 2012 Conference on Smart Materials, Adaptive Structures and Intelligent Systems (SMASIS)*, Stone Mountain, Georgia, USA, 2012.

[10] F. Gandhi and S.-G. Kang, "Beams with controllable flexural stiffness," *Smart Materials and Structures*, vol. 16, pp. 1179–1184, 2007.

[11] W. Raither, A. Bergamini, F. Gandhi, and P. Ermanni, "Adaptive bending-twist coupling in laminated composite plates by controllable shear stress transfer," *Composites Part A: Applied Science and Manufacturing*, vol. 43, no. 10, pp. 1709–1716, 2012.

[12] W. Raither, A. Bergamini, and P. Ermanni, "Profile beams with adaptive bending-twist coupling by adjustable shear center location," in *22nd International Conference on Adaptive Structures Technologies (ICAST2011)*, Corfu, Greece, 2011.

[13] L. H. Sperling, *Introduction to Physical Polymer Science*. Hoboken: John Wiley & Sons, 2005.

[14] H. Schlichting and E. Truckenbrodt, *Aerodynamik des Flugzeuges. Erster Band*, 3rd ed. Berlin: Springer, 2001.

[15] M. Drela. (2012, July) XFOIL 6.97. [Online]. Available: http://web.mit.edu/drela/Public/web/xfoil/

[16] "Type-Certificate. Data Sheet. ASW 27," EASA, 2008.

[17] J. D. Anderson, *Fundamentals of Aerodynamics*. New York: McGraw-Hill, 2001.

[18] "Advanced Composites Group MTM 44-1 Data Sheet," 2008.

[19] "Technical data. Epoxy resin L," R&G Faserverbundwerkstoffe, 2010.

[20] "Araldite® LY 5052/Aradur® 5052," Huntsman Switzerland, 2007.

[21] G. Kress. (2012) CAP. Composites Analysis Program.

[22] C. C. Chamis, *Engineer's Guide to Composite Materials*. ASM, 1987, ch. Simplified composite micromechanics equations for mechanical, thermal, and moisture-related properties.

[23] H. Schürmann, *Konstruieren mit Faser-Kunststoff-Verbunden*. Berlin: Springer, 2005.

[24] *Plastics – Determination of tensile properties – Part 1: General principles (ISO/DIS 527-1:2010)*, Deutsches Institut für Normung, DIN/EN/ISO Std., 2010.

[25] *Plastics – Determination of tensile properties – Part 2: Test conditions for moulding and extrusion plastics (ISO/DIS 527-2:2010)*, Deutsches Institut für Normung, DIN/EN/ISO Std., 2010.

[26] E. Baur, S. Brinkmann, T. Osswald, and E. Schmachtenberg, *Saechtling Kunststoff-Taschenbuch*. München: Carl Hanser Verlag, 2007.

[27] G. Becker and D. Braun, *Kunststoff-Handbuch. Polyvinylchlorid*, H. Felger, Ed. München: Carl Hanser Verlag, 1986.

[28] "RIM 624. RIM-Polyurethanharz," Axson Technologies, 2005.